remote sensing

MDPI

Article

Downscaling Land Surface Temperature from MODIS Dataset with Random Forest Approach over Alpine Vegetated Areas

Paulina Bartkowiak [1,2,*], Mariapina Castelli [1] and Claudia Notarnicola [1]

[1] Eurac Research, Institute for Earth Observation, 39100 Bolzano, Italy; mariapina.castelli@eurac.edu (M.C.); claudia.notarnicola@eurac.edu (C.N.)

[2] Department of Earth and Environmental Sciences, University of Milano-Bicocca, Piazza della Scienza 1 e 4, I-20126 Milano, Italy

* Correspondence: paulina.bartkowiak@eurac.edu; Tel.: +39-3272-203-972

Received: 24 April 2019; Accepted: 30 May 2019; Published: 1 June 2019

Abstract: In this study, we evaluated three different downscaling approaches to enhance spatial resolution of thermal imagery over Alpine vegetated areas. Due to the topographical and land-cover complexity and to the sparse distribution of meteorological stations in the region, the remotely-sensed land surface temperature (LST) at regional scale is of major area of interest for environmental applications. Even though the Moderate Resolution Imaging Spectroradiometer (MODIS) LST fills the gap regarding high temporal resolution and length of the time-series, its spatial resolution is not adequate for mountainous areas. Given this limitation, random forest algorithm for downscaling LST to 250 m spatial resolution was evaluated. This study exploits daily MODIS LST with a spatial resolution of 1 km to obtain sub-pixel information at 250 m spatial resolution. The nonlinear relationship between coarse resolution MODIS LST (CR) and fine resolution (FR) explanatory variables was performed by building three different models including: (i) all pixels (BM), (ii) only pixels with more than 90% of vegetation content (EM1) and (iii) only pixels with 75% threshold of homogeneity for vegetated land-cover classes (EM2). We considered normalized difference vegetation index (NDVI) and digital elevation model (DEM) as predictors. The performances of the thermal downscaling methods were evaluated by the Root Mean Square Error (RMSE) and the Mean Absolute Error (MAE) between the downscaled dataset and Landsat LST. Validation indicated that the error values for vegetation fraction (EM1, EM2) were smaller than for basic modelling (BM). BM model determined averaged RMSE of 2.3 K and MAE of 1.8 K. Enhanced methods (EM1 and EM2) gave slightly better results yielding 2.2 K and 1.7 K for RMSE and MAE, respectively. In contrast to the EMs, BM showed a reduction of 22% and 18% of RMSE and MAE respectively with regard to Landsat and the original MODIS LST. Despite some limitations, mainly due to cloud contamination effect and coarse resolution pixel heterogeneity, random forest downscaling exhibits a large potential for producing improved LST maps.

Keywords: thermal downscaling; MODIS; land surface temperature; random forest; modelling

1. Introduction

In this study, we used MODIS datasets to increase spatial resolution of the land surface temperature (LST) images in the Alpine region. We performed modelling by using the digital elevation model (DEM) and normalized difference vegetation index (NDVI) as a set of predictors of 250 m spatial resolution (FR), and the 1 km resolution LST product (CR) as a dependent variable. This paper analyses the strength of random forest downscaling (RFD) using different variants for model creation. With the

use of different approaches, it was possible to examine in which way explanatory variables explain the spatio-temporal LST distribution within the study area.

Thermal remote sensing has significantly contributed to the enhancement of spatio-temporal information about temperature distribution on the surface of the Earth. One of the key possibilities provided by satellite instruments is data acquisition in the thermal infrared (TIR) domain, from which land surface thermal conditions are derived [1–3]. Land surface temperature (LST) retrieved from remote sensing data at different scales is an essential variable in environmental research studies, e.g., in agricultural management [4–7], in urban heat island assessment [8–12], for evapotranspiration (ET) modelling [13–18] and drought monitoring [5,6,19].

National Oceanic and Atmospheric Administration-Advanced Very High Resolution Radiometer (NOAA-AVHRR) and Moderate Resolution Imaging Spectroradiometer (MODIS) images with daily temporal resolution have improved the quality of continuous Earth monitoring, however their moderate spatial resolution is not sufficient to perform analyses in areas characterized by high spatial heterogeneity in terms of topography and land-cover. Contrary to the aforementioned instruments, thermal images acquired by fine spatial resolution scanners installed on different satellites (e.g., Landsat 5, Landsat 8) are more effective in spatial pattern detection [20–22]. There is still a limitation in the existing satellite instruments since numerous satellites provide data at high spatial resolution but with non-satisfactory repeat cycle (e.g., 16-day revisit time for Landsat) [13,23]. In recent studies [14,24,25] associated with application of thermal remote sensing for continuous evapotranspiration modelling, the authors indicate the need to retrieve data at both high spatial resolution and short repeat cycle. Therefore, in the above-mentioned applications, TIR imagery with both small pixel size and high temporal resolution is highly desirable [26]. Among existing methods for LST pixel size enhancement, downscaling technique is one of the most commonly used approaches in many research studies [27,28].

Thermal downscaling is a technique to retrieve a new LST dataset at finer spatial resolution than original one based on independent variables that represent biophysical properties obtained by remotely-sensed data at higher spatial resolution. This technique exploits the correlation between co-registered fine resolution (FR) with long revisit time and coarse resolution (CR) with short revisit time data to obtain images with both small pixel size and short revisit time. In order to provide improved LST maps, regression modelling is performed based on aggregated independent variables and LST maps. For a better characterization of thermal variations on the Earth surface, it is common to use fine spatial resolution data in modelling, such as individual spectral reflectance bands in visible and infrared electromagnetic regions, spectral indices, digital elevation models or land-use/land-cover (LULC) information [29–33].

The robustness of downscaling methods for analyzing land surface thermal conditions in different landscapes has been well demonstrated in literature. Most of the studies related to LST downscaling concentrate on statistical thermal sharpening techniques exploiting vegetation-based spectral indices (VIs). VIs offer a satisfactory base for exploring relationships between LST and biophysical properties of different land-cover types because of the correlation between land surface temperature and spectral vegetation response [34–37]. The most widely-used method is Disaggregation Procedure for Radiometric Surface Temperature (DisTrad) algorithm which exploits performance of spectral indices to investigate their correlation with thermal bands [24]. In order to disaggregate land surface temperature pixels to the shortwave band resolution, Kustas et al. [24] assume that there is a least-square fitting between NDVI and TIR. Because of the original DisTrad limitations related to ill-defined NDVI distributions over complex regions, some modifications were introduced in the preliminary concept. Agam et al. [25] developed a technique for thermal sharpening (TsHARP) replacing NDVI by fractional vegetation cover (Fv), for which the correlation coefficients were higher compared to the ones obtained with simple spectral indices. Using high biomass area in the study, Qiu et al. [38] introduced a refinement evaluating a new spectral index in the DisTrad model and showed that performance of enhanced vegetation index (EVI) for LST sub-pixel mapping was a more robust approach for LST modelling.

Classical methods used successfully for topographically uniform areas and relatively homogenous land-cover are not efficient in complex regions [39,40]. Therefore, application of other explanatory variables instead of individual VI-based predictors has been performed in many studies [40–44]. As shown by Bechtel et al. [42], the introduction of additional parameters, such as averaged TIR images, land-cover based products or data obtained from image dimensionality reduction (e.g., Principle Component Analysis, PCA), improved the goodness-of-fit in the modelling. Many authors suggested that the application of simple multivariate modelling increases the accuracy of LST downscaling. Results obtained by Maeda [29] demonstrated that when applying DEM in combination with NDVI, higher coefficients of determination ($R^2 \geq 0.95$) were observed. Furthermore, Duan & Li [43] proposed successfully to use LST, NDVI and altitude in geographically weighted regression (GWR) to eliminate stationary effect affected by simple univariate and multivariate regression approaches.

Although traditional statistical techniques seem to be promising in many case studies, some authors suggest the use of machine learning techniques in order to take into account the non-linearity between predictors and LST [41,45]. Even if we exploit more mathematically complex regressions, machine learning methods can incorporate many explanatory variables in the physical-deterministic modelling. Furthermore, due to the use of machine learning in thermal sharpening, automatic data production shows more robust results. Therefore, different techniques have been exploited, including Bayesian-based modelling [46], support vector regression [47], artificial neural networks [48] and random forests (RF) [39,49]. Pioneers in the use of RF technique for downscaling purposes were Hutengs & Vohland [39] who developed sharpening of simulated Landsat thermal maps with ground sampling distance (GSD) equals to 60 and 120 m to retrieve Landsat-like images of VNIR spatial resolution (GSD = 30 m). The authors applied multi-source data fusion in the model, including reflectance bands and DEM products over vegetated areas, yielding good model performance. No method was universally recognized as better than the others, though RF modelling is a promising technique over terrain influenced by multiple factors.

Since there are few studies related to thermal sub-pixel mapping for complex topography, the novelty of the paper is to implement RF image sharpening to overcome LST limitations for mountainous ecosystems by taking into account topographic features and land-cover heterogeneity [29,39,50]. Due to evolving meteorological conditions, the Alps are a hot spot of climate change and of drought extreme events. Thus, TIR remotely-sensed data at fine spatial resolution are highly desirable.

This paper consists of the following paragraphs: Section 2 shows information about data used and describes methodology as well as the applied RF downscaling algorithm, Section 3 presents evaluation of the results. The last two paragraphs deal with discussion related to the study findings and conclusion for the whole paper.

2. Materials and Methods

2.1. Study Area

The study area is located in the central-eastern Alps in the northern part of Italy, the Autonomous Province of Bolzano/Bozen, and it covers area of 7400 km^2 (Figure 1).

The region is predominantly mountainous, divided from north to south by the Adige/Etsch river valley. Elevation ranges from 110 m to about 3685 m a.s.l. The mountainous topography determines land-cover heterogeneity. The region is mainly covered by forests, grasslands, pastures and agricultural areas. Due to complexity of the environment and topographical location, the Province of Bolzano/Bozen is one of the driest areas in the Alps with diversified microclimate zones [51]. The climate type is differentiated depending on geographical location; sub-continental for the main valleys, continental in the mountain valleys and alpine within the regions above forest border [50].

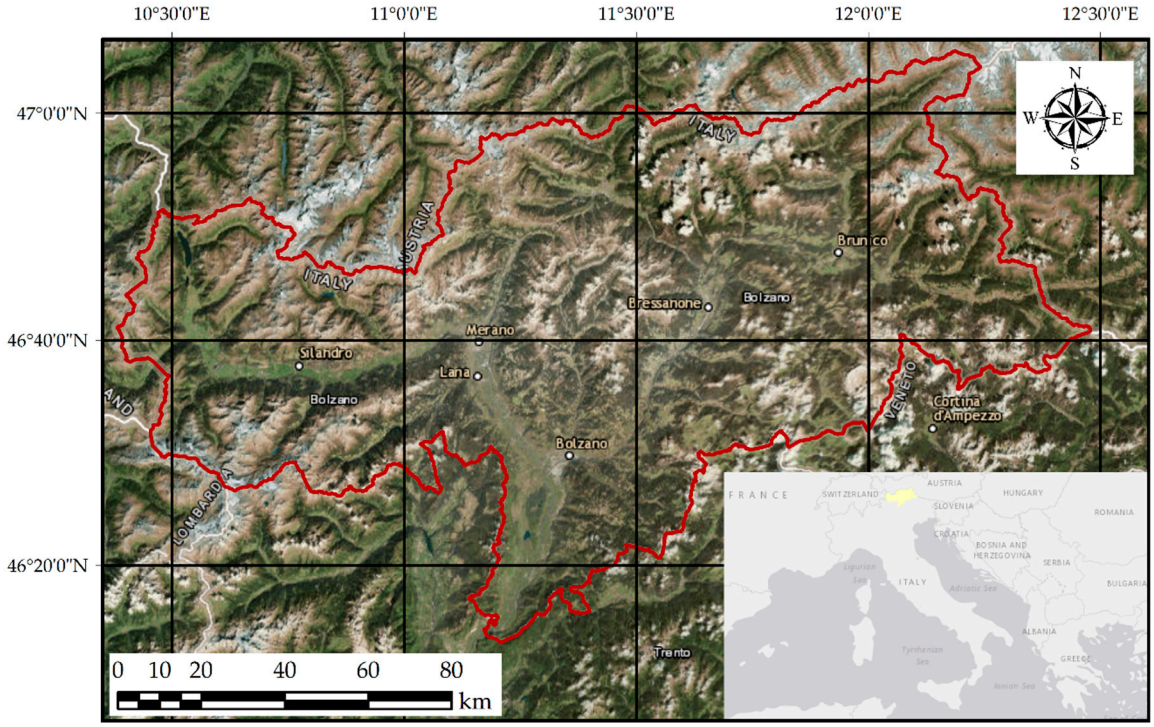

Figure 1. Geographical location of the study area (source: map was created using ArcGIS® software by Esri. ArcGIS® and ArcMap™ are the intellectual property of Esri and are used herein under license. Copyright © Esri).

2.2. Input Data

In this study we used as coarse resolution input (CR) MODIS/Terra– the MOD11A1.006 Land Surface Temperature (LST) product [52], daily at 1 km spatial resolution, and MODIS/Terra and Aqua NDVI 4-Day composites (see Table 1 for details), at 250 m spatial resolution [53]. Since our main aim is to evaluate downscaling possibilities over vegetated areas, we selected imagery within vegetation phenological cycle, from April to November. MODIS data were acquired from April 2003 to June 2017. The data were produced and qualified in this time frame during the MONALISA project [53]. The grids were originally obtained in MODIS Sinusoidal projection (SR-ORG: 6974). The MOD11A1 products were subset and downloaded from Google Earth Engine, and consisted of daytime surface temperature distribution with an accuracy of approximately 1 K [54]. To get cloud uncontaminated image collection, before data downloading we applied the bitmask using JavaScript API available in Google Earth Engine platform. Only imagery with good quality flag (QA) was used in the study. The 4-Day NDVI MODIS data produced by Eurac research within the MONALISA project [55] included composites created with the use of Maximum Value Composite (MVC) algorithm for all vegetated areas (according to Corine Land Cover 2012) from MODIS/Aqua and Terra images (MOD/MYD09GQ and 09GA Version 6) [56–59]. The final dataset consisted in time-series of images from 2003 to 2017, from April to November, months with green vegetation cover.

Table 1. Overview of original and processed datasets in this study.

Dataset Name	Spatial Resolution	Short Description	Derivatives Products
MOD11A1	1000 m	MODIS Terra Land Surface Temperature	Resampled to NDVI spatial resolution (GSD = 250 m) for residual correction
NDVI 4-Day composites	250 m	MODIS Terra and MODIS Aqua Reflectance bands based on MOD09GA	NDVI aggregated to 1000 m pixel size by spatial averaging
ASTER GDEM	30 m	Global Digital Elevation Model acquired ASTER scanner	GDEM resampled to 250 m and 1000 m spatial resolution
LISS 2013 -Land Information System South Tyrol	-	Land Information System South Tyrol based on GeoEye-1 image collection from 2012	Vegetation vector masks for: - areas covered by minimum 90% of vegetation within 1km pixels - pure pixels for different types of vegetation (75% threshold of homogeneity)
Landsat 5	30 m 120 m (30) [2]	Atmospherically-corrected reflectance products (red, NIR), Thermal at-sensor radiance	Gaussian filtering and resampling to 250 m
Landsat 8	30 m 100 m (30) [2]	Atmospherically-corrected reflectance products (red, NIR), Thermal at-sensor radiance	Gaussian filtering and resampling 250 m
MOD05_L2	1000 m	MODIS Precipitable Water	Re-projected to MODIS Sinusoidal Projection

[1] GSD: Ground Sampling Distance. [2] resampled products by data provider.

In order to evaluate the performances of the proposed downscaling method in the area of interest, we validated our results with Landsat images (WRS-2 Path: 192, Row: 28) reprojected to MODIS Sinusoidal Projection (Table 2). Data applied for the algorithm were retrieved through the NASA Earthdata explorer [60] and the Level-1 and Atmosphere Archive & Distribution System (LAADS) Distributed Active Archive Center (DAAC). The acquired multispectral images in VNIR domain are characterized by Surface Reflectance Level-2, while thermal bands are characterized by Level-1, therefore a pre-processing was needed. We selected for the validation Landsat images with the same acquisition dates as MODIS Terra LST. The time difference between Landsat (Landsat 5 and Landsat 8) and MODIS Terra LST composites did not exceed 1.5 hours. Due to the lack of good quality data caused by common cloud contamination and shadows effects, we selected seven time-coincident Landsat (Table 2) and seven MODIS LST (MOD11A1) images with the corresponding 4-day NDVI Terra/Aqua combined composites (Table 1) acquired in different seasons. To perform the atmospheric correction of Landsat thermal bands we used MODIS Water Vapor product (MOD05_L2) [61,62]. To retrieve Landsat LST maps, we performed three main steps: (i) calculation of the at-sensor brightness temperature (T_B) and of NDVI, (ii) calculation of emissivity (ε) based on vegetation fraction [62] and (iii) land surface temperature retrieval [61,62].

Table 2. Landsat dataset used in the validation process.

Date	Sensor	Granule ID	Overpass Time (GMT)
27.09.2004	Landsat 5 TM	LT05_L1TP_192028_20040927_20161129_01_T1	09:42
25.05.2005		LT05_L1TP_192028_20050525_20161126_01_T1	09:45
16.10.2005		LT05_L1TP_192028_20051016_20161124_01_T1	09:46
18.07.2007		LT05_L1TP_192028_20070718_20161112_01_T1	09:52
12.09.2010		LT05_L1TP_192028_20100912_20161013_01_T1	09:48
27.08.2016	Landsat 8 TIRS	LC08_L1TP_192028_20160827_20170321_01_T1	09:58
11.06.2017		LC08_L1TP_192028_20170611_20170627_01_T1	09:58

For the downscaling procedure, in addition to MODIS NDVI, we used information on elevation provided by the Global Digital Elevation Model (GDEM), acquired by the Advanced Spaceborne

Thermal Emission and Reflection Radiometer (ASTER), at approximately 30 m resolution [63]. For the original dataset we performed bilinear resampling to a resolution of 250 m and then we applied spatial averaging to 1000-m pixel using mean function within 4 × 4 kernel size [39].

To select and characterize vegetated areas, in this study we exploited the LULC vector layers based on high spatial resolution RapidEye imagery (GSD = 6.5 m) of 2012, produced by the Institute for Earth Observation of Eurac research in the frame of the project "LISS-2013—Land-use information in South Tyrol: update, harmonization with European Standards and integration of research results" (© Autonome Provinz Bozen – Südtirol | 28.0.1 Landeskartographie und Koordination der Geodaten). This dataset includes minimum polygon at the level of 1600 m^2, contrary to the more commonly used Corine Land Cover (CLC) database, for which the minimum area of individual object is 25 ha. An overview of the datasets used in the study is shown in Table 1.

2.3. Methodology

2.3.1. The Random Forest Algorithm

RF regression is a machine learning technique exploiting statistical nonlinear relationship between variables. This dataset required for RF regression consists of observations (n), including predictors (p) and dependent variable. Basic component of random forest algorithm is regression tree, and the main concept is to build many different subsets. Randomness is introduced by the fact that each tree is created based on random sample with replacement of n from training data (bootstrap sample). The method determines the best split by increasing similarity between features in each sub-node. One method to achieve this is to minimize variance or to reduce standard deviation of variables on the basis of random sample. In practice, p/3 of randomly sampled variables is used as split candidates. No pruning is applied when constructing the trees, which means any split is removed from the model. Random forest predictions are calculated for each regression tree separately and then arithmetic average of the trees as final forecast is performed. Basic equation describing final RF prediction for regression results based on created trees is presented as follows:

$$F(x) = \frac{\sum_{j=1}^{N} T_j(x)}{N} \quad (1)$$

where N indicates number of trees, T_j represents each tree and F is a prediction at a new point x as an averaged prediction based on created trees [64].

Since the random forest regression divides dataset into decorrelated trees and then predicts a target variable based on average value obtained from the subsets, it is robust for high dimensional grid data [65]. RF regression is considered easy in optimization by applying a relatively small number of parameters in modelling. Random forest procedure requires specifying a few user parameters, including tree quantity and minimum number of observations in each tree [64,65]. Many authors showed that RF regression enables to use continuous dataset as well as categorized predictors, such as land-cover information [39]. In theory, a RF model can explain LST values by multivariate relationship, considering different inputs, like remotely-sensed spectral indices, incoming solar radiation, digital elevation models, terrain slope and aspect, land-cover maps or soil moisture [39,49].

2.3.2. Implementation of Random Forest for Thermal Sharpening

MODIS Land Surface Temperature, with its spatial resolution of 1 km, does not provide accurate spatial information for many environmental analyses performed within specific land-cover types at the level of individual regions and municipalities [13,14]. Therefore, in this study, the random forest algorithm was selected to model the relationship between the 1 km MODIS LST and the 250-m DEM and time-coincident 4-days composites of MODIS NDVI. Downscaling procedure was implemented in R software and GDAL Utilities using packages intended for that purpose [66–69].

Apart from the spectral indices, it is known that for mountainous areas topography variations have a large impact on vegetation types and phenology. Because of adiabatic temperature differences vegetation cover changes with elevation, which results in diversified flora zones. Furthermore, height gradients lead to big biodiversity of spatially distributed land-cover and therefore it influences LST distribution [70]. For this reason, in this work we modelled the relationship between low resolution daytime LST imagery and spatial information at 250 m pixel size, including NDVI and digital elevation model.

After resampling DEM to NDVI resolution, we performed mean aggregation on FR data to simulate parameters of CR dataset. Next, random forest regression was carried out. The number of trees was set to 1000 based on a "trial & error" approach as a compromise between processing burden and accuracy [4,71]. The whole downscaling procedure was based on the relationship between coarse resolution images and then applied to the FR pixels. Modelling was based on the following relationship:

$$LST_{CR} = f\left(NDVI_{FR_{deg}}\ ,\ DEM_{FR_{deg}}\right) \quad (2)$$

where the subscript *CR* means variable at coarse resolution and the subscript FR_{deg} indicates degraded fine resolution predictors to 1000 m pixel size, with f a nonlinear function of combined altitude and NDVI established by the RF method.

When finishing RF regressions for a single image from the image collection, models were applied to 250-m pixels to predict FR land surface temperature maps. Consequently, simulated FR LST values were obtained using the following Equation (3):

$$LST_{FR} = f(NDVI_{FR}\ ,\ DEM_{FR}) \quad (3)$$

To approximate scale effect on the correlation between LST and predictors, many authors [39,41,72] have used residual correction originally implemented by Kustas et al. [24]. This operation involves the following steps: (i) aggregation by averaging of FR LST images to original MODIS LST pixel size, (ii) residuals calculation (Δ) by subtracting re-aggregated fine resolution LST pixels (LST_{FRdeg}) from original LST images (LST_{CR}), (iii) CR residuals resampling to LST_{FR}-like spatial resolution and adding these corrections to LST predictions from modelling (LST_{FR}), as shown in Equation (5):

$$\Delta = LST_{CR} - LST_{FR_{deg}} \quad (4)$$

$$LST_{FR_{res}} = LST_{FR} + \Delta \quad (5)$$

where LST_{FRres} indicates simulated LST pixels at 250 m spatial resolution after addition of residual correction.

2.3.3. Random Forest Model Concepts

Due to topography complexity and land-cover heterogeneity in the Alpine region, prior to final selection of predictors we tested explanatory performance of different variables, including NDVI, DEM, aspect, sky view factor maps as well as MODIS near-infrared bands. NDVI and DEM were selected in the estimation of land surface temperature variations dependent on altitude as they showed to be the most relevant predictors. We tested the model as well based on all the predictors and we found that on average the difference among the two models was around 0.71 K.

Moreover, we evaluated three different approaches: (i) basic modelling (BM), (ii) enhanced modelling 1 (EM1) and (iii) enhanced modelling 2 (EM2). In the BM method all good quality pixels covering the study area were applied in RFD. It means that pixels including different land-cover types within squares of 1 km length were exploited for the image sharpening [39]. The two latter model concepts arise from the need to retrieve homogeneity characteristics at initial MODIS LST scale. In terms of homogenous pixels-based downscaling we evaluated regressions for every vegetated land cover class within the region, including forest, vineyards and orchards, annual crops, grassland and bushes.

As reported by Kustas et al. [24] and then by Essa et al. [73], the selection of homogenous low-resolution pixels improves correlation results between spectral indices and LST. Therefore, we conducted RFD using EM1-based approach as a piecewise modelling regarding fractional vegetation cover and then we applied stricter criteria to the third model, including only pure pixels (EM2). Contrary to BM, EM1 is a more advanced disaggregation method based only on pixels mostly covered by vegetation. The selection of pixels at low spatial resolution allowed extracting data that exhibit a certain degree of homogeneity. Since not all pixels contained vegetation, we applied a threshold of 90% for vegetation within 1 km pixel-based mask (EM1) and then using 75% homogeneity criteria based on vegetation classes obtained from the LISS 2013 (EM2). The last model assumed that pixels within the same vegetation class should be similar, considering spectral- and spatial-neighborhood patterns. In this way the model EM2 represents areas with full homogeneity characteristics.

Based on the above-mentioned thresholds we applied three LST prediction approaches within 1-km fishnet pixel-based mask. Due to high level of heterogeneity and common cloud contamination effect in the Alpine region, many pixels were excluded from further analysis. The performed image sub-pixel sharpening approach is summarized in Figure 2.

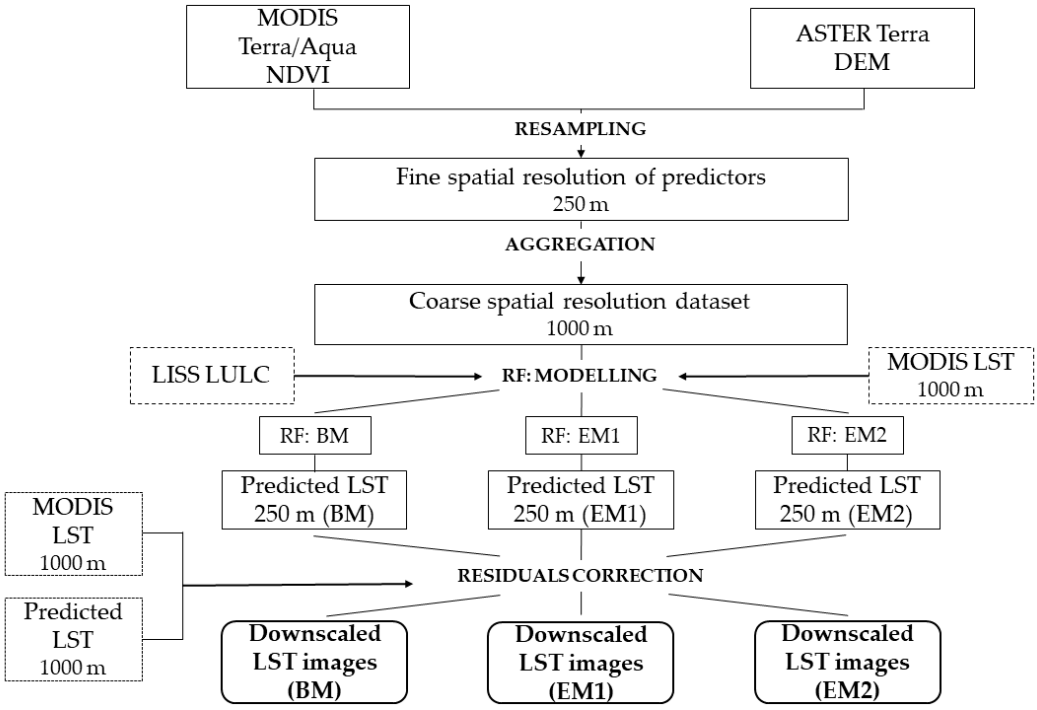

Figure 2. Overview of the procedure for downscaling land surface temperature from MODIS data.

2.3.4. Data Preparation for the Validation Phase

To assess RF modelling performance, we calculated Root Mean Square Error (RMSE) and Mean Absolute Error (MAE) between the downscaled MODIS LST and Landsat LST degraded to 250 m pixel size. We calculated RMSE and MAE as follows:

$$RMSE = \sqrt{\frac{\sum_{j=1}^{N}(LST_{FR_{res}} - LST_{Lt})^2}{N}}; MAE = \frac{\sum_{j=1}^{N}\left|LST_{FR_{res}} - LST_{Lt}\right|}{N} \quad (6)$$

where N is the number of observations, and subscript of Lt indicates land surface temperature for Landsat pixels degraded to downscaled MODIS-like spatial resolution.

To assess the model performances, we validated our results by using Landsat imagery acquired in different seasons. Downscaled LST images were validated with the use of Landsat 5 TM and Landsat 8

TIRS LST maps having a common extent of MODIS tiles. The Landsat dataset was resampled to 250 m pixel size to simulate the CR data.

After applying residuals calculated on the basis of Equations (4) and (5), we processed the Landsat dataset to retrieve LST at 250 m spatial resolution. Different approaches have been used to atmospherically correct satellite-based thermal data [74–76]. Among various techniques, the Single Channel (SC) algorithm has been widely applied as an efficient method for LST retrieval [61,77]. In this study we applied the SC of Jiménez Muñoz et al. [71]. This LST retrieval method is based on the following general formula developed by Jiménez-Muñoz et al. [62]:

$$LST = \gamma\left[\frac{1}{\varepsilon}(\psi_1 L + \psi_2) + \psi_3\right] + \delta \quad (7)$$

where ψ_1, ψ_2, ψ_3 are derived from MODIS water vapor content for each sensor separately [77], and γ, δ are given by:

$$\gamma = \left\{\frac{c_2 L}{T_B^2}\left[\frac{\lambda^4}{c_1}L + \lambda^{-1}\right]\right\}^{-1} \; ; \; \delta = -\gamma L + T_B \quad (8)$$

where L is at-satellite radiance, c_1 and c_2 are sensor constants, λ indicates the effective wavelength of thermal bands.

Atmospheric water vapor content (WV) for the Landsat acquisition dates (Table 2) did not exceed 3 g cm^{-2}. Based on tests conducted by Sobrino & El Kharraz [78], MODIS water vapor product (MOD05_L2) with WV concentration smaller than 3 g cm^{-2} is reliable input in Single Channel LST retrieval. According to authors, SC algorithm based on MOD05_L2 at maximum level of 3 g cm^{-2}, provides RMSE values of about 1.5 K [61,77].

After applying smoothing Gaussian filtering and mean value cell area weighted resampling for upscaling, we calculated LST maps for the selected dates [39]. Landsat images used for the validation are summarized in Table 2.

3. Results

3.1. Global Validation

As mentioned before, to evaluate the effectiveness of the BM, EM1 and EM2 random forest regression, we conducted spatial degradation of TIR bands from Landsat 5 and Landsat 8 to downscaled MODIS 250 m pixel size (Table 1). Moreover, a comparison with MODIS LST at 1000 m is carried out in order to understand what is the level of improvement obtained with the downscaling procedure. Since this paper is intended for vegetation analyses, RMSE and MAE were calculated for seven sharpened images acquired in different seasons (spring, summer, autumn). Figure 3 shows RMSE and MAE for the proposed model, averaged in the study area.

As can be observed, random forest algorithm, regardless of pixel selection method, was able to predict sub-pixel LST with similar accuracy. All disaggregation methods based on fractional vegetation mask slightly improved the accuracy of the downscaled 250 m LST layouts. Overall RMSEs (MAEs) ranged from 1.81 K to 2.51 K (1.39 K to 1.91 K) for EM1 and 1.66 K to 2.67 K (1.18 K to 2.16 K) for enhanced modelling 2. Uniform modelling (BM) yielded RMSE values from 1.90 K to 2.58 K and MAE from 1.45 K to 1.97 K, respectively. The largest RMSE was found for LST image dated on 27 September 2004 ($RMSE_{BM}$ = 2.58 K, $RMSE_{EM1}$ = 2.51 K). Similar situation applied to MAE evaluation index (MAE_{BM} = 1.95 K, MAE_{EM1} = 1.88 K), which corresponded to an accuracy improvement of 4% compared to BM.

Regression performances differed depending on acquisition date. Apart from images acquired in September and October, we achieved a positive effect of enhanced modelling (EM1, EM2) on the accuracy results (Figure 3). The greatest errors appeared for the scenes from early autumn (27 September 2004) and from late spring (11 June 2017), with RMSE of about 2.6 K and 2.4 K, respectively.

Such discrepancies, documented in Figure 3, may have occurred because of different periods of growing season, the limited number of samples and their small variability incorporated in the RF modelling. This is likely due to weather conditions during image acquisitions, with dense cloud cover and shadowed surfaces over the Alps. These factors influenced negatively the determination of the impact of biomass content and elevation in the prediction of land surface temperature spatial patterns.

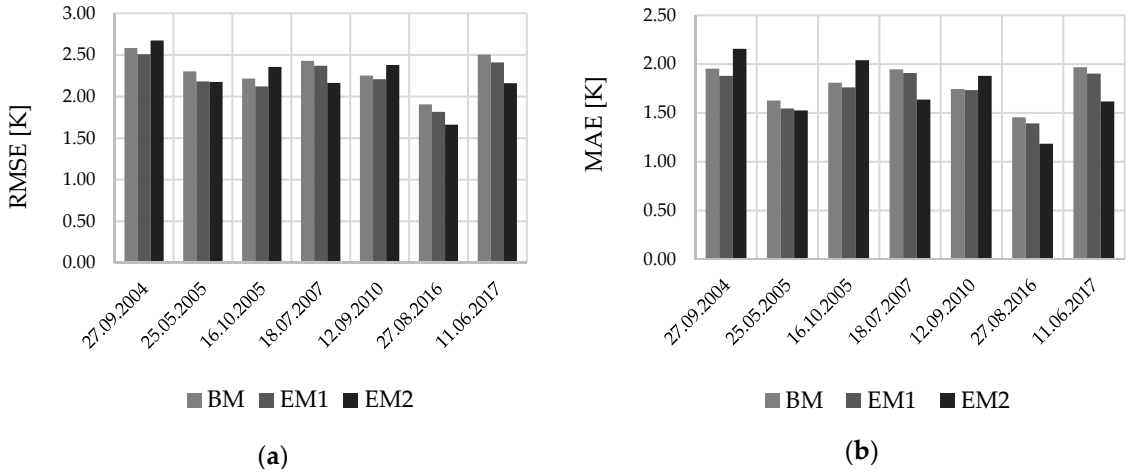

Figure 3. Validation results based on average Root Mean Square Error (RMSE) (**a**) and Mean Absolute Error (MAE) (**b**) between disaggregated images and reference images for Basic Modelling (BM), Enhanced Modelling 1 (EM1), and Enhanced Modelling 2 (EM2).

Similar behavior in the context of models' performances presents scatterplot comparison of the downscaled MODIS LST and Landsat references (Figures 3 and 4). The graphs created for dates with the highest and the lowest global RMSEs and MAEs (Figure 3) show almost the same spatial distributions for all the exploited approaches. The graphs indicate that different vegetation thresholds for applied models did not introduce noticeable improvements (Figure 4).

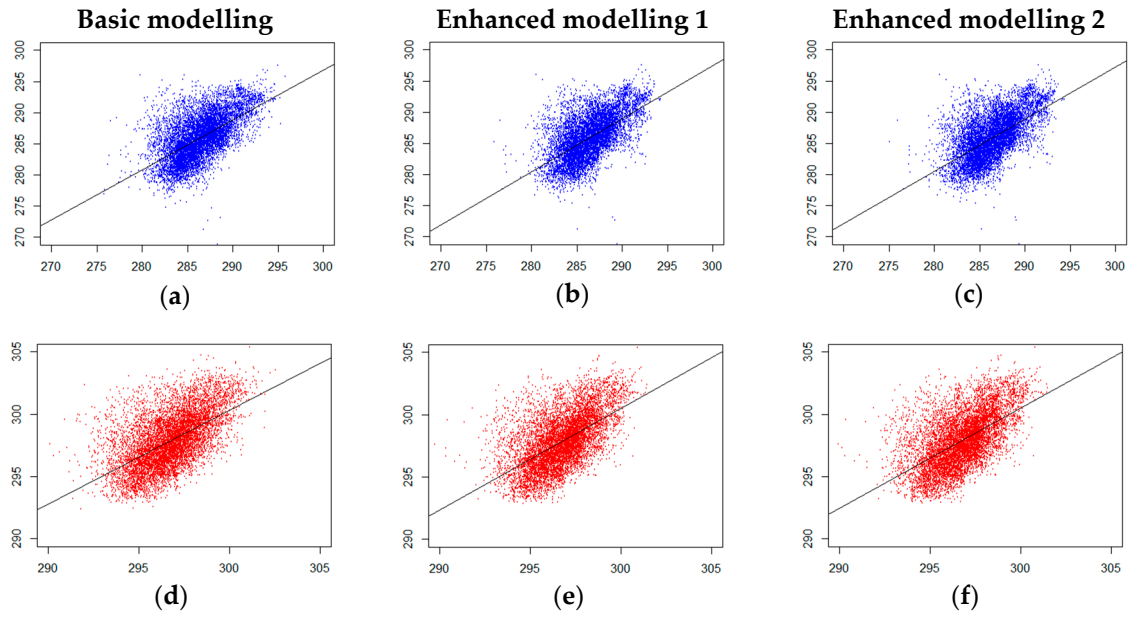

Figure 4. Scatterplots of the sharpened MODIS land surface temperature (LST) [K] [**X-axis**] versus Reference Image [K] [**Y-axis**] (degraded Landsat LST) for the applied RF models (BM, EM1, EM2). The top row shows results obtained on 27 September 2004 (**a**–**c**) and the lower line presents outcomes for 27 August 2016 (**d**–**f**).

Considering the averaged global analysis, we achieved better results for BM with disaggregated MODIS LST than for the original datasets (Table 3). EM1 and EM2 yielded quite similar RMSE and MAE values, which indicates a reduced contribution of different variables incorporated in both LST sharpening methods. In contrast to the latter methods, $RMSE_{mean}$ (MAE_{mean}) for basic modelling was equal to 2.31 K (1.79 K), which corresponded to accuracy improvement of 22% (18%) compared to statistics obtained for Landsat and the original MODIS (Table 3). The above-mentioned outcomes (Figures 3 and 4) indicate that the proposed RF approaches gave quite similar LST spatial patterns.

Table 3. Overview of averaged Root Mean Square Error (RMSE) and Mean Absolute Error (MAE) ($RMSE_{mean}$, MAE_{mean}) based on all Landsat validation data at global scale.

Landsat LST vs. original MODIS LST			**Landsat LST vs. sharpened MODIS LST**		
$RMSE_{mean}$					
BM	EM1	EM2	BM	EM1	EM2
2.97	2.38	2.44	2.31	2.23	2.22
MAE_{mean}					
BM	EM1	EM2	BM	EM1	EM2
2.18	1.83	1.85	1.79	1.73	1.72

In addition to the assessment of the model performances provided by RMSE and MAE, we conducted a qualitative assessment of the results based on visual analysis for the methods used, by comparing downscaled LST with original MODIS LST at 1 km resolution and with Landsat LST downgraded at 250 m resolution (Figure 5).

Differences in spatial patterns between the original MODIS and the downscaled imagery can be noticed (Figure 5b–e). This behavior is especially visible for the valleys within the study area. Notable visual improvements are noticeable in the north east valleys for which Landsat-like thermal variability with higher LST values was obtained (Figure 5c). Based on qualitative assessment, downscaling procedures allow identifying finer details. In contrast to the enhanced approaches (EM1, EM2), larger number of samples regarding BM modelling influenced bigger variability of downscaled pixels (Figure 5c–e). Comparing Landsat LST after applying vegetation mask (Figure 5a) with the downscaled MODIS Terra LST products (Figure 5c–e), we observed that sharpened pixels showed similar distribution triggered by the original CR imagery (Figure 5b). The above-mentioned outcomes (Figures 3–5) indicate that the proposed RF approaches gave similar LST spatial patterns as well. In most cases degraded Landsat LST maps had a broader temperature value distribution than the original MODIS LST at 1 km spatial resolution. This means that RFD affected by CR LST data could not be able to simulate thermal variations at sub-pixel level over the area (e.g., on 27 September 2004, Landsat LST values ranged from 258.6 K to 298.7 K and MODIS LST values ranged from 277.6 K to 294.6 K).

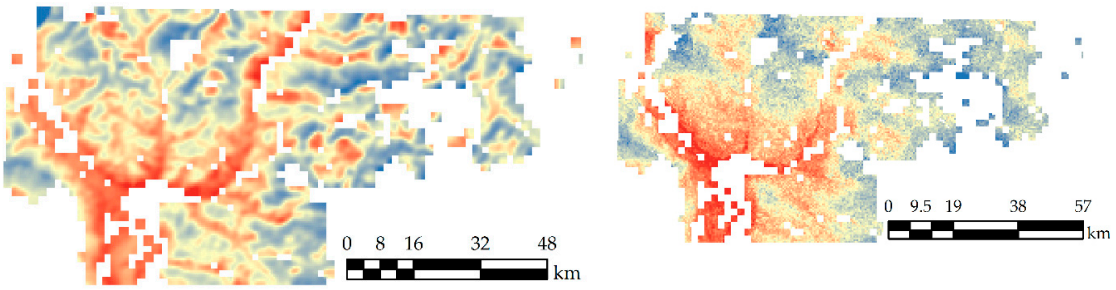

(**a**) (**c**)

Figure 5. *Cont.*

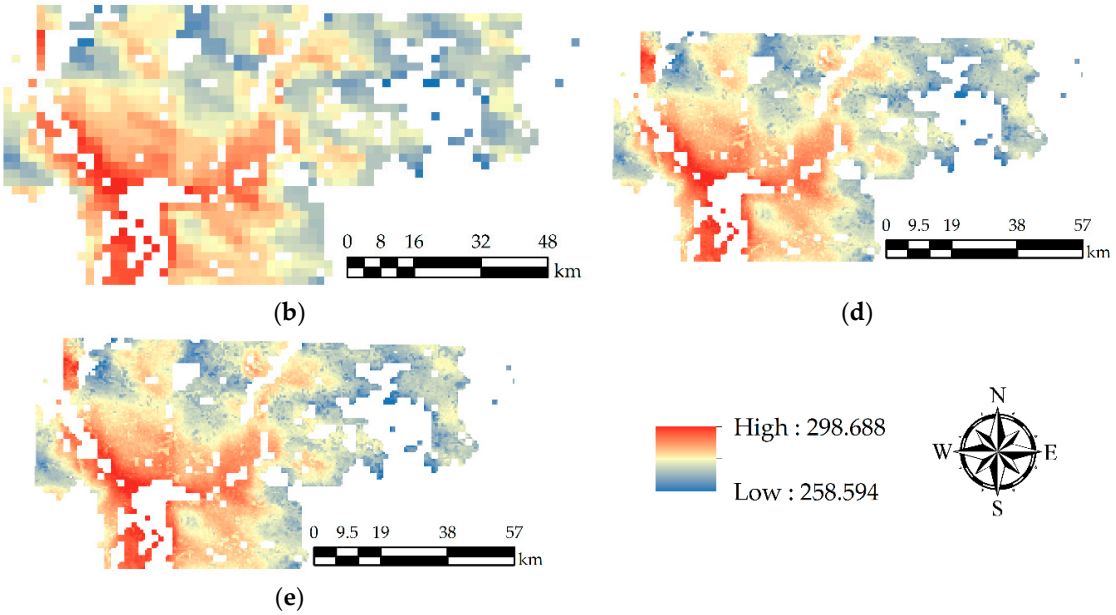

Figure 5. Visual comparison between MODIS images and the time-coincident Landsat LST maps degraded to 250 m spatial resolution. The left column shows: (**a**) degraded Landsat reference image (250 m), and (**b**) the original MODIS LST (1000 m), and the right column corresponds to downscaled imagery sharpened by BM (**c**), EM1 (**d**), EM2 (**e**) on 27 September 2004.

3.2. *Validation for the Different Land Cover Classes*

In parallel with the global validation, to assess the influence of land-cover type on model results we performed the validation based on the RMSEs for each vegetated class obtained from LISS resources. Additionally, the original MODIS LST was compared against degraded Landsat LST products. Due to better performance obtained for basic modelling (Table 3), in Tables 4 and 5 we show BM prediction errors for five LULC, including forest, vineyards and orchards, annual crops, grassland and bushes.

Table 4. Local comparison of RMSE between reference images and sharpened MODIS data obtained by basic modelling (BM) for different land-cover types.

Landsat LST vs. Sharpened MODIS LST						
RMSE (K)						
Date	**Forest**	**Vineyards & Orchards**	**Annual Crops**	**Grassland**	**Bushes**	**AVERAGE**
27.09.2004	2.57	2.55	2.19	3.03	3.53	2.78
25.05.2005	1.84	2.67	1.24	3.30	5.09	2.83
16.10.2005	2.19	1.45	1.05	2.50	4.08	2.25
18.07.2007	2.10	4.33	3.60	2.95	3.26	3.25
12.09.2010	2.10	2.66	2.97	2.78	3.36	2.77
27.08.2016	1.58	2.39	2.47	2.66	3.22	2.46
11.06.2017	2.09	3.32	4.13	3.38	4.43	3.47
AVERAGE	2.07	2.77	2.52	2.94	3.85	-

Table 5. Local comparison of RMSE between reference images and original MODIS data obtained by BM approach.

Landsat LST vs. original MODIS LST						
RMSE (K)						
Date	**Forest**	**Vineyards & Orchards**	**Annual Crops**	**Grassland**	**Bushes**	**AVERAGE**
27.09.2004	2.73	2.75	2.30	3.53	3.85	3.03
25.05.2005	1.96	2.46	1.03	4.05	5.51	3.00
16.10.2005	2.24	1.62	2.71	3.06	4.64	2.86
18.07.2007	2.20	3.98	3.02	3.32	3.91	3.29
12.09.2010	2.21	2.56	3.41	3.30	4.57	3.21
27.08.2016	1.65	2.11	2.02	3.05	3.67	2.50
11.06.2017	2.19	2.97	3.23	3.85	4.48	3.34
AVERAGE	2.17	2.64	2.53	3.45	4.38	-

As can be seen in the above tables (Tables 4 and 5), at the level of different vegetation types, accuracies of thermal downscaling are diversified and therefore RMSE values increased in many cases. Considering global and local evaluation measures, we found that larger deviations between downscaled/original MODIS LST and Landsat LST were obtained at land-cover level. Regarding the size of RMSE values, the BM yielded less satisfactory results for bush class, for which standard deviation ranged 0.63–0.71 K and the $RMSE_{mean}$ was 3.85 K for sharpened MODIS and 4.38 K for the original MODIS (Tables 4 and 5). Due to the complicated structure of vineyards and orchards, which influence sub-pixel variability, RMSE ranged from 1.45 K to 4.33 K. A similar behavior was observed on 11 July 2017 for annual crops, grassland and bushes classes yielding maximum RMSE errors of BM ranging from 3.23 K to 4.48 K (Tables 4 and 5). On average, for the forest class the prediction error (Table 4) was markedly lower ($RMSE_{mean}$ = 2.17 K), corresponding to an improvement of 2–6% in prediction accuracies (RMSE) against the original MODIS LST (Table 5). Despite bigger RMSE and MAE values than for other classes, the largest improvements after downscaling were observed for grasslands and bushes yielding 15% and 12% decreases in RMSE, respectively. As already noted for the global comparison, the BM at local scale did improve accuracy outcomes. On average, differences in $RMSE_{BM}$ between the original MODIS and the downscaled outcomes ranged from −0.13 K to 0.60 K. Only $RMSE_{mean}$ ($RMSE_{mean}$ = −0.13 K) for 11 June 2017 indicated lack of improvements in the RFD procedure.

4. Discussion

The proposed random forest algorithm allows predicting LST at the medium spatial resolution (250 m) yielding satisfactory results. Model performance assessment based on quantitative comparison between MODIS original and downscaled images showed BM as more robust method than other approaches. Considering the applied random forest models (BM, EM1, EM2) exploiting DEM and NDVI explanatory performance, findings from this study indicate that prediction error differences between downscaled images obtained by different implementation of RF regressions were insignificant (Figure 3, Table 3). Regardless of number of prediction variables and masks applied, differences in RMSEs between BM and EMs on average did not exceed 0.1 K. In this case the outcomes from the paper are not in agreement with results obtained by Kustas et al. [24] who showed that purity pixel selection caused improvement in downscaling procedure as a big potential for spatial ET modelling. When comparing the prediction errors (Figure 3) to the ones observed by Merlin et al. [79], Jeganathan et al. [41], Maeda [29] and Hutengs & Vohland [39], we noted that our evaluation measures had on average lower values. Hutengs & Vohland [39] applied random forest regression to MODIS LST data with RMSEs ranging from 1.41 K to 1.92 K. Similarly, good results were obtained by Maeda [29]. The author showed that by using simple multivariate regression (DEM and NDVI as predictors) it was possible to downscale daytime 1-km images with maximum standard error equals to 3.29 K and

coefficient of determination, R^2_{min} = 0.78. Above-mentioned results are site-dependent and are highly influenced by topographic complexity as well as by vegetation heterogeneity over study area.

RFD exhibits a large potential for producing enhanced LST maps, despite some limitations, mainly due to cloud contamination and heterogeneity of 1-km pixels. In fact, within 2003–2017 image collection, the unavoidable presence of contaminated pixels may have impact on the final quality of the downscaling outputs. Furthermore, since the downscaled images maintained the spatial characteristics of the original 1 km thermal data, the possibility of extracting homogenous pixels based on vegetation cover fraction is hampered.

Vegetation content in the Alpine region is differentiated, meaning that within 1 km fishnet based on MODIS LST many pixels were not dominated by vegetation. Since in today's research on downscaling techniques many authors have shown that the introduction of a big number of predictors improves model performance [39,49], our preliminary model concept included diversified explanatory variables, like topography-derived variables (terrain slope and aspect) and reflectance bands. Nonetheless, by introducing these additional data we achieved similar resampled Landsat-downscaled MODIS relationship and, as a result, we obtained the same spatial information as with the predictors which we have chosen. Moreover, the exploitation of masks derived from the LISS land-cover, based on vegetation content thresholds, led to similar mean prediction errors both generally and for single land-cover classes. Based on preliminary tests, the high precision of the vector layer did not improve the 250 m outputs with a difference ranging from 0.5 to 1.1 K. Therefore, for the application of the proposed method to larger areas, Corine Land Cover maps with a Minimum Mapping Unit (MMU) of 25 ha could be an alternative to LISS 2013.

Statistical comparison between 250 m spatial resolution Landsat LST and the sharpened as well as the original MODIS LST maps provided an overview for the assessment of the downscaling accuracy. By applying Gaussian filtering and then upscaling resampling to Landsat LST it was possible to partially smooth spatial details registered by high resolution sensors. However, there were still some LST discrepancies caused by complex terrain affected by thermal anisotropy, changeable meteorological conditions between time acquisitions or different viewing angle of sensors. Another issue was related to uniformly disaggregated MODIS residuals which kept spatial information at CR pixel base. Thus, future work will focus on the development of residual correction based on its normalization prior to applying it to predicted pixels [30,32].

Unfortunately, due to the lack of ground data for the chosen Landsat acquisitions (Table 2), comparison of the results with field measurements was not conducted. Future work should include multiple ground-based radiometric measurements, distributed spatially in order to incorporate LST values for different land cover classes within test sites.

As shown in Table 3, since there is a high level of agreement between the three applied model concepts, further evaluation of random forest should be considered. The spectral response for heterogeneous areas of the Alps represents various biomes, which are spatially and temporarily limited. Due to the common cloud contamination over the study area, it was not possible to combine these methods with data acquired from different sensors, such as Landsat 8 TIRS-1. On the other hand, by using high spatial resolution data for the downscaling procedure and then applying FR mask, it would be more effective to retrieve thermal contrast within smaller pixels corresponding to different materials. Given this approach, heterogeneity of LULC could be overcome by extraction of spectrally pure grid cells representing unique vegetated land-cover classes. This could bring to significant accuracy improvements for random forest modelling over the complex area of the Autonomous Province of Bolzano/Bozen.

5. Conclusions

This study presents an evaluation of the random forest algorithm for downscaling MODIS LST, based on the relationship between land surface temperature and static and dynamic variables, including digital elevation model and NDVI, in the heterogeneous ecosystems of the Alps. The

application of three RF model concepts was needed to investigate whether the selection of specific pixels based on land-cover criteria contributed to explain LST distribution over the Province of Bolzano/Bozen. This paper demonstrates that RF machine learning regression, regardless of the method used, was capable of modelling non-linear relationships between variables in a very robust way.

The performance of the proposed regressions (BM, EM1, EM2) against co-registered Landsat images yielded quite similar results. A comparison based on statistical measures indicated that, on average, RMSE (MAE) ranged from 1.66 K to 2.67 K (from 1.18 K to 2.16 K). At level of single land cover classes, temperature deviations were also observed with significant LST differences for grasslands and bushes (Tables 4 and 5).

Considering these difficulties, further studies should firstly focus on the implementation of approaches to predict missing pixels, in order to perform LST downscaling based on full image coverage and enhance modelling robustness. Future work will also concentrate on the development of improved LST sharpening methods to reduce the gap between FR data with low temporal resolution and coarse resolution imagery acquired at daily basis. Considering the recent progress in the availability of satellites acquiring FR imagery, such as Landsat and Sentinel missions; further modifications of the LST downscaling will exploit these datasets, which is an urgent need for studies related to climatology, drought monitoring, and water management. These activities require high spatial resolution datasets to retrieve detailed information about spatial variability of LST. Considering this issue, downscaling procedures exploiting both MODIS LST and new high spatial resolution space-borne instruments have a large potential for regional water availability assessments.

Author Contributions: Conceptualization, P.B., M.C. and C.N.; Methodology, P.B.; Formal analysis, P.B.; Investigation, P.B.; Writing—original draft preparation, P.B.; Writing—review and editing, P.B., M.C. and C.N.; Supervision, M.C., C.N.

Funding: This study has been carried out within the project "Cyclamen" financed by Provincia Autonoma di Bolzano, Alto Adige/Süd Tirol, Ripartizione Diritto allo studio, Università e ricerca scientifica, within the scope of Provincial Law 14 from 13. December 2006 (Project Nr. 5/34).

Acknowledgments: The authors thank the Department of Innovation, Research and University of the Autonomous Province of Bozen/Bolzano for covering the Open Access publication costs.

Conflicts of Interest: The authors declare no conflict of interest. The funders had no role in the design of the study; in the collection, analyses, or interpretation of data; in the writing of the manuscript, or in the decision to publish the results.

References

1. Czajkowski, K.P.; Goward, S.N.; Mulhern, T.; Goetz, S.J.; Walz, A.; Shirey, D.; Dubayah, R.O. Estimating environmental variables using thermal remote sensing. In *Thermal Remote Sensing in Land Surface Processes*; Quattrochi, D.A., Luvall, J.C., Eds.; CRC Press LLC: Boca Raton, FL, USA, 2004; pp. 11–32.
2. Weng, Q. Thermal infrared remote sensing for urban climate and environmental studies: Methods, applications, and trends. *ISPRS J. Photogramm.* **2009**, *64*, 335–344. [CrossRef]
3. Niclòs, R.; Tomás, S.; Juan, M.; Valiente, J.A.; Barberà, M.J.; Caselles, D.; Caselles, V. *Evaluation of Landsat-8 Thermal Bands to Monitor Land Surface Temperature*; Serie A; Publicaciones de la Asociación Española de Climatología: Sevilla, Spain, 2014; Volume 9.
4. Park, S.; Im, J.; Jang, E.; Rhee, J. Drought assessment and monitoring through blending of multi-sensor indices using machine learning approaches for different climate regions. *Agric. For. Meteorol.* **2016**, *216*, 157–169. [CrossRef]
5. Swain, S.; Wardlow, B.D.; Narumalani, S.; Tadesse, T.; Callahan, K. Assessment of vegetation response to drought in Nebraska using Terra-MODIS land surface temperature and normalized difference vegetation index. *GISci. Remote Sens.* **2011**, *48*, 432–455. [CrossRef]
6. Anderson, M.C.; Zolin, C.A.; Sentelhas, P.C.; Hain, C.R.; Semmens, K.; Yilmaz, M.T.; Tetrault, R. The Evaporative Stress Index as an indicator of agricultural drought in Brazil: An assessment based on crop yield impacts. *Remote Sens. Environ.* **2016**, *174*, 82–99. [CrossRef]

7. Anderson, M.C.; Hain, C.; Wardlow, B.; Pimstein, A.; Mecikalski, J.R.; Kustas, W.P. Evaluation of drought indices based on thermal remote sensing of evapotranspiration over the continental United States. *J. Clim.* **2011**, *24*, 2025–2044. [CrossRef]
8. Voogt, J.A.; Oke, T.R. Thermal remote sensing of urban climates. *Remote Sens. Environ.* **2003**, *86*, 370–384. [CrossRef]
9. Lu, D.; Song, K.; Zang, S.; Jia, M.; Du, J.; Ren, C. The effect of urban expansion on urban surface temperature in Shenyang, China: An analysis with landsat imagery. *Environ. Model. Assess.* **2015**, *20*, 197–210. [CrossRef]
10. Balçik, F.B. Determining the impact of urban components on land surface temperature of Istanbul by using remote sensing indices. *Environ. Monit. Assess.* **2014**, *186*, 859–872. [CrossRef]
11. Hardy, C.H.; Nel, A.L. Data and techniques for studying the urban heat island effect in Johannesburg. In Proceedings of the International Archives of Photogrammetry, Remote Sensing and Spatial Information Sciences, Berlin, Germany, 11–15 May 2015; Volume XL-7/W3, p. 203.
12. Deilami, K.; Kamruzzaman, M. Modelling the urban heat island effect of smart growth policy scenarios in Brisbane. *Land Use Policy* **2017**, *64*, 38–55. [CrossRef]
13. Anderson, M.C.; Allen, R.G.; Morse, A.; Kustas, W.P. Use of Landsat thermal imagery in monitoring evapotranspiration and managing water resources. *Remote Sens. Environ.* **2012**, *122*, 50–65. [CrossRef]
14. Castelli, M.; Anderson, M.C.; Yang, Y.; Wohlfahrt, G.; Bertoldi, G.; Niedrist, G.; Notarnicola, C. Two-source energy balance modeling of evapotranspiration in Alpine grasslands. *Remote Sens. Environ.* **2018**, *209*, 327–342. [CrossRef]
15. Tang, R.; Li, Z.L. Evaluation of two end-member-based models for regional land surface evapotranspiration estimation from MODIS data. *Agric. For. Meteorol.* **2015**, *202*, 69–82. [CrossRef]
16. Rahimi, S.; Gholami Sefidkouhi, M.A.; Raeini-Sarjaz, M.; Valipour, M. Estimation of actual evapotranspiration by using MODIS images (a case study: Tajan catchment). *Arch. Agron. Soil Sci.* **2015**, *61*, 695–709. [CrossRef]
17. Anderson, M.C.; Norman, J.M.; Mecikalski, J.R.; Otkin, J.A.; Kustas, W.P. A climatological study of evapotranspiration and moisture stress across the continental United States based on thermal remote sensing: 1. Model formulation. *J. Geophys. Res. Atmos.* **2007**, *112*. [CrossRef]
18. Carpintero, E.; Dugo, M.G.; Hain, C.; Nieto, H.; Gao, F.; Andreu, A.; Anderson, M.C. Continuous evapotranspiration monitoring and water stress at watershed scale in a Mediterranean oak savanna. In *Remote Sensing for Agriculture, Ecosystems, and Hydrology XVIII*; International Society for Optics and Photonics: Leiden, The Netherlands, 2016; Volume 9998, p. 99980N.
19. Park, S.; Feddema, J.J.; Egbert, S.L. Impacts of hydrologic soil properties on drought detection with MODIS thermal data. *Remote Sens. Environ.* **2004**, *89*, 53–62. [CrossRef]
20. Xing, Q.; Li, L.; Lou, M.; Bing, L.; Zhao, Z.; Li, Z. Observation of oil spills through Landsat thermal infrared imagery: A case of deepwater horizon. *Aquat. Procedia* **2015**, *3*, 151–156. [CrossRef]
21. Semmens, K.A.; Anderson, M.C.; Kustas, W.P.; Gao, F.; Alfieri, J.G.; McKee, L.; Xia, T. Monitoring daily evapotranspiration over two California vineyards using Landsat 8 in a multi-sensor data fusion approach. *Remote Sens. Environ.* **2016**, *185*, 155–170. [CrossRef]
22. Allan, M.G.; Hamilton, D.P.; Trolle, D.; Muraoka, K.; McBride, C. Spatial heterogeneity in geothermally-influenced lakes derived from atmospherically corrected Landsat thermal imagery and three-dimensional hydrodynamic modelling. *Int. J. Appl. Earth Obs.* **2016**, *50*, 106–116. [CrossRef]
23. Wulder, M.A.; White, J.C.; Loveland, T.R.; Woodcock, C.E.; Belward, A.S.; Cohen, W.B.; Roy, D.P. The global Landsat archive: Status, consolidation, and direction. *Remote Sens. Environ.* **2016**, *185*, 271–283. [CrossRef]
24. Kustas, W.P.; Norman, J.M.; Anderson, M.C.; French, A.N. Estimating subpixel surface temperatures and energy fluxes from the vegetation index–radiometric temperature relationship. *Remote Sens. Environ.* **2003**, *85*, 429–440. [CrossRef]
25. Agam, N.; Kustas, W.P.; Anderson, M.C.; Li, F.; Neale, C.M. A vegetation index based technique for spatial sharpening of thermal imagery. *Remote Sens. Environ.* **2007**, *107*, 545–558. [CrossRef]
26. Weng, Q.; Fu, P.; Gao, F. Generating daily land surface temperature at Landsat resolution by fusing Landsat and MODIS data. *Remote Sens. Environ.* **2014**, *145*, 55–67. [CrossRef]
27. Zurita-Milla, R.; Kaiser, G.; Clevers, J.G.; Schneider, W.; Schaepman, M.E. Downscaling time series of MERIS full resolution data to monitor vegetation seasonal dynamics. *Remote Sens. Environ.* **2009**, *113*, 1874–1885. [CrossRef]
28. Atkinson, P.M. Downscaling in remote sensing. *Int. J. Appl. Earth Obs.* **2013**, *22*, 106–114. [CrossRef]

29. Maeda, E.E. Downscaling MODIS LST in the East African mountains using elevation gradient and land-cover information. *Int. J. Remote Sens.* **2014**, *35*, 3094–3108. [CrossRef]
30. Bindhu, V.M.; Narasimhan, B.; Sudheer, K.P. Development and verification of a non-linear disaggregation method (NL-DisTrad) to downscale MODIS land surface temperature to the spatial scale of Landsat thermal data to estimate evapotranspiration. *Remote Sens. Environ.* **2013**, *135*, 118–129. [CrossRef]
31. Bisquert, M.; Sánchez, J.M.; Caselles, V. Evaluation of disaggregation methods for downscaling MODIS land surface temperature to Landsat spatial resolution in Barrax test site. *IEEE J. Sel. Top. Appl.* **2016**, *9*, 1430–1438. [CrossRef]
32. Essa, W.; Verbeiren, B.; van der Kwast, J.; Batelaan, O. Improved DisTrad for Downscaling Thermal MODIS Imagery over Urban Areas. *Remote Sens.* **2017**, *9*, 1243. [CrossRef]
33. Lillo-Saavedra, M.; García-Pedrero, A.; Merino, G.; Gonzalo-Martín, C. 2018 TS2uRF: A New Method for Sharpening Thermal Infrared Satellite Imagery. *Remote Sens.* **2018**, *10*, 249. [CrossRef]
34. Zhou, X.; Wang, Y.C. Dynamics of Land Surface Temperature in Response to Land-Use/Cover Change. *Geogr. Res.* **2011**, *49*, 23–36. [CrossRef]
35. Wan, Z.; Wang, P.; Li, X. Using MODIS land surface temperature and normalized difference vegetation index products for monitoring drought in the southern Great Plains, USA. *Int. J. Remote Sens.* **2004**, *25*, 61–72. [CrossRef]
36. Yue, W.; Xu, J.; Tan, W.; Xu, L. The relationship between land surface temperature and NDVI with remote sensing: Application to Shanghai Landsat 7 ETM+ data. *Int. J. Remote Sens.* **2007**, *28*, 3205–3226. [CrossRef]
37. Karnieli, A.; Agam, N.; Pinker, R.T.; Anderson, M.; Imhoff, M.L.; Gutman, G.G.; Goldberg, A. Use of NDVI and land surface temperature for drought assessment: Merits and limitations. *J. Clim.* **2010**, *23*, 618–633. [CrossRef]
38. Qiu, J.; Yang, J.; Wang, Y.; Su, H. A comparison of NDVI and EVI in the DisTrad model for thermal sub-pixel mapping in densely vegetated areas: A case study in Southern China. *Int. J. Remote Sens.* **2018**, *39*, 2105–2118. [CrossRef]
39. Hutengs, C.; Vohland, M. Downscaling land surface temperatures at regional scales with random forest regression. *Remote Sens. Environ.* **2016**, *178*, 127–141. [CrossRef]
40. Mukherjee, S.; Joshi, P.K.; Garg, R.D. A comparison of different regression models for downscaling Landsat and MODIS land surface temperature images over heterogeneous landscape. *Adv. Space Res.* **2014**, *54*, 655–669. [CrossRef]
41. Jeganathan, C.; Hamm, N.A.S.; Mukherjee, S.; Atkinson, P.M.; Raju, P.L.N.; Dadhwal, V.K. Evaluating a thermal image sharpening model over a mixed agricultural landscape in India. *Int. J. Appl. Earth Obs.* **2011**, *13*, 178–191. [CrossRef]
42. Bechtel, B.; Zakšek, K.; Hoshyaripour, G. Downscaling land surface temperature in an urban area: A case study for Hamburg, Germany. *Remote Sens.* **2012**, *4*, 3184–3200. [CrossRef]
43. Duan, S.B.; Li, Z.L. Spatial downscaling of MODIS land surface temperatures using geographically weighted regression: Case study in northern China. *IEEE Trans. Geosci. Remote* **2016**, *54*, 6458–6469. [CrossRef]
44. Zhang, X.; Zhao, H.; Yang, J. Spatial downscaling of land surface temperature in combination with TVDI and elevation. *Int. J. Remote Sens.* **2019**, *40*, 1875–1886. [CrossRef]
45. Chen, Y.; Zhan, W.; Quan, J.; Zhou, J.; Zhu, X.; Sun, H. Disaggregation of Remotely sensed land surface temperature: A generalized paradigm. *IEEE Trans. Geosci. Remote Sens.* **2014**, *52*, 5952–5965. [CrossRef]
46. Fasbender, D.; Tuia, D.; Bogaert, P.; Kanevski, M.F. Support-Based Implementation of Bayesian Data Fusion for Spatial Enhancement: Applications to ASTER Thermal Images. *IEEE Geosci. Remote Sens.* **2008**, *5*, 598–602. [CrossRef]
47. Keramitsoglou, I.; Kiranoudis, C.T.; Weng, Q. Downscaling geostationary land surface temperature imagery for urban analysis. *IEEE Geosci. Remote Sens.* **2013**, *10*, 1253–1257. [CrossRef]
48. Bai, Y.; Wong, M.S.; Shi, W.Z.; Wu, L.X.; Qin, K. Advancing of land surface temperature retrieval using extreme learning machine and spatio-temporal adaptive data fusion algorithm. *Remote Sens.* **2015**, *7*, 4424–4441. [CrossRef]
49. Yang, Y.; Cao, C.; Pan, X.; Li, X.; Zhu, X. Downscaling Land Surface Temperature in an Arid Area by Using Multiple Remote Sensing Indices with Random Forest Regression. *Remote Sens.* **2017**, *9*, 789. [CrossRef]
50. Neteler, M. Estimating daily land surface temperatures in mountainous environments by reconstructed MODIS LST data. *Remote Sens.* **2010**, *2*, 333–351. [CrossRef]

51. Isotta, F.A.; Frei, C.; Weilguni, V.; Perčec Tadić, M.; Lassegues, P.; Rudolf, B.; Munari, M. The climate of daily precipitation in the Alps: Development and analysis of a high-resolution grid dataset from pan-Alpine rain-gauge data. *Int. J. Climatol.* **2014**, *34*, 1657–1675. [CrossRef]
52. Wan, Z.; Hook, S.; Hulley, G. *MOD11A1 MODIS/Terra Land Surface Temperature/Emissivity Daily L3 Global 1km SIN Grid V006*; NASA EOSDIS LP DAAC; NASA: Washington, DC, USA, 2015.
53. Asam, S.; Callegari, M.; Matiu, M.; Fiore, G.; De Gregorio, L.; Jacob, A.; Menzel, A.; Zebisch, M.; Notarnicola, C. Relationship between Spatiotemporal Variations of Climate, Snow Cover and Plant Phenology over the Alps—An Earth Observation-Based Analysis. *Remote Sens.* **2018**, *10*, 1757. [CrossRef]
54. Wan, Z. *MODIS Land-Surface Temperature Algorithm Theoretical Basis Document (LST ATBD)*; Institute for Computational Earth System Science: Santa Barbara, CA, USA, 1999; p. 75.
55. MONALISA. Available online: http://www.monalisa-project.eu (accessed on 20 December 2018).
56. Vermote, E.; Wolfe, R. *MOD09GQ MODIS/Terra Surface Reflectance Daily L2G Global 250 m SIN Grid V006*; NASA EOSDIS LP DAAC; NASA: Washington, DC, USA, 2015.
57. Vermote, E.; Wolfe, R. *MYD09GQ MODIS/Aqua Surface Reflectance Daily L2G Global 250 m SIN Grid V006*; NASA EOSDIS LP DAAC; NASA: Washington, DC, USA, 2015.
58. Vermote, E.; Wolfe, R. *MOD09GA MODIS/Terra Surface Reflectance Daily L2G Global 1 km and 500 m SIN Grid V006*; NASA EOSDIS LP DAAC; NASA: Washington, DC, USA, 2015.
59. Vermote, E.; Wolfe, R. *MYD09GA MODIS/Aqua Surface Reflectance Daily L2G Global 1 km and 500 m SIN Grid V006*; NASA EOSDIS LP DAAC; NASA: Washington, DC, USA, 2015.
60. EARTHDATA Search. Available online: https://search.earthdata.nasa.gov (accessed on 10 November 2018).
61. Jiménez-Muñoz, J.C.; Sobrino, J.A.; Skoković, D.; Mattar, C.; Cristóbal, J. Land surface temperature retrieval methods from Landsat-8 thermal infrared sensor data. *IEEE Geosci. Remote Sens.* **2014**, *11*, 1840–1843. [CrossRef]
62. Jiménez-Muñoz, J.C.; Cristóbal, J.; Sobrino, J.A.; Sòria, G.; Ninyerola, M.; Pons, X. Revision of the single-channel algorithm for land surface temperature retrieval from Landsat thermal-infrared data. *IEEE Trans. Geosci. Remote* **2009**, *47*, 339–349. [CrossRef]
63. *NASA/METI/AIST/Japan Spacesystems, and U.S./Japan ASTER Science Team ASTER Global Digital Elevation Model [Version 2, 49oN, 6oE]*; NASA EOSDIS Land Processes DAAC; NASA: Washington, DC, USA, 2009.
64. Hastie, T.; Tibshirani, R.; Friedman, J. Random forests. In *The Elements of Statistical Learning*; Series in Statistics; Springer: New York, NY, USA, 2001; pp. 587–602.
65. Breiman, L. Random forests. *Mach. Learn.* **2001**, *45*, 5–32. [CrossRef]
66. GDAL/OGR Contributors. *GDAL/OGR Geospatial Data Abstraction Software Library*; Open Source Geospatial Foundation: Chicago, IL, USA, 2019; Available online: https://gdal.org (accessed on 20 December 2018).
67. Hijmans, R.J. Raster: Geographic Data Analysis and Modeling. R Package Version 2.8-19. 2019. Available online: https://CRAN.R-project.org/package=raster (accessed on 20 December 2018).
68. Liaw, A.; Wiener, M. Classification and Regression by randomForest. *R News* **2002**, *2*, 18–22.
69. Bivand, R.; Keitt, T.; Rowlingson, B. Rgdal: Bindings for the 'Geospatial' Data Abstraction Library; R Package Version 0.8-16. Available online: http://CRAN.R-project.org/package=rgdal (accessed on 20 December 2018).
70. Barry, R.G. *Mountain Weather and Climate*; Psychology Press: Hove, UK, 1992.
71. Li, M.; Im, J.; Beier, C. Machine learning approaches for forest classification and change analysis using multi-temporal Landsat TM images over Huntington Wildlife Forest. *GISci. Remote Sens.* **2013**, *50*, 361–384. [CrossRef]
72. Chen, X.; Li, W.; Chen, J.; Rao, Y.; Yamaguchi, Y. A combination of TsHARP and thin plate spline interpolation for spatial sharpening of thermal imagery. *Remote Sens.* **2014**, *6*, 2845–2863. [CrossRef]
73. Essa, W.; van der Kwast, J.; Verbeiren, B.; Batelaan, O. Downscaling of thermal images over urban areas using the land surface temperature–impervious percentage relationship. *Int. J. Appl. Earth Obs.* **2013**, *23*, 95–108. [CrossRef]
74. Yu, X.; Guo, X.; Wu, Z. Land surface temperature retrieval from Landsat 8 TIRS—Comparison between radiative transfer equation-based method, split window algorithm and single channel method. *Remote Sens.* **2014**, *6*, 9829–9852. [CrossRef]
75. Sattari, F.; Hashim, M. A brief review of land surface temperature retrieval methods from thermal satellite sensors. *Middle-East J. Sci. Res.* **2014**, *22*, 757–768.

76. Dissanayake, D.; Morimoto, T.; Murayama, Y.; Ranagalage, M. Impact of Landscape Structure on the Variation of Land Surface Temperature in Sub-Saharan Region: A Case Study of Addis Ababa using Landsat Data (1986–2016). *Sustainability* **2019**, *11*, 2257. [CrossRef]
77. Sobrino, J.A.; Jimenez-Munoz, J.C.; Paolini, L. Land surface temperature retrieval from LANDSAT TM 5. *Remote Sens. Environ.* **2004**, *90*, 434–440. [CrossRef]
78. Sobrino, J.A.; El Kharraz, J.; Li, Z.L. Surface temperature and water vapour retrieval from MODIS data. *Int. J. Remote Sens.* **2003**, *24*, 5161–5182. [CrossRef]
79. Merlin, O.; Duchemin, B.; Hagolle, O.; Jacob, F.; Coudert, B.; Chehbouni, G.; Kerr, Y. Disaggregation of MODIS surface temperature over an agricultural area using a time series of Formosat-2 images. *Remote Sens. Environ.* **2010**, *114*, 2500–2512. [CrossRef]